

Estimating small angular scale CMB anisotropy with high resolution N-body simulations: weak lensing

M.J. Fullana¹, J.V. Arnau², R.J. Thacker³, H.M.P. Couchman⁴, and D. Sáez⁵

diego.saez@uv.es

Received _____; accepted _____

¹Institut de Matemàtica Multidisciplinària, Universitat Politècnica de València, 46022 València, Spain

²Departamento de Matemática Aplicada, Universidad de Valencia, 46100 Burjassot, Valencia, Spain

³Department of Astronomy and Physics, Saint Mary's University, Halifax, Nova Scotia, B3H 3C3 Canada

⁴Department of Physics and Astronomy, McMaster University, 1280 Main St. West, Hamilton, Ontario, L8S 4M1, Canada

⁵Departamento de Astronomía y Astrofísica, Universidad de Valencia, 46100 Burjassot, Valencia, Spain

ABSTRACT

We estimate the impact of weak lensing by strongly nonlinear cosmological structures on the cosmic microwave background. Accurate calculation of large ℓ multipoles requires N-body simulations and ray-tracing schemes with both high spatial and temporal resolution. To this end we have developed a new code that combines a gravitational Adaptive Particle-Particle, Particle-Mesh (AP3M) solver with a weak lensing evaluation routine. The lensing deviations are evaluated while structure evolves during the simulation so that all evolution steps—rather than just a few outputs—are used in the lensing computations. The new code also includes a ray-tracing procedure that avoids periodicity effects in a universe that is modeled as a 3-D torus in the standard way. Results from our new simulations are compared with previous ones based on Particle-Mesh simulations. We also systematically investigate the impact of box volume, resolution, and ray-tracing directions on the variance of the computed power spectra. We find that a box size of $512h^{-1}$ Mpc is sufficient to provide a robust estimate of the weak lensing angular power spectrum in the ℓ -interval (2,000–7,000). For a realistic cosmological model the power $[\ell(\ell + 1)C_\ell/2\pi]^{1/2}$ takes on values of a few μK in this interval, which suggests that a future detection is feasible and may explain the excess power at high ℓ in the BIMA and CBI observations.

Subject headings: methods:numerical — cosmic background radiation — cosmology:theory — large-scale structure of the universe

1. Introduction

Photons from the last scattering surface of the cosmic microwave background (CMB) detected at redshift zero, are inevitably lensed by cosmological structures. This lensing produces a number of modifications to the CMB angular power spectrum, deviations from Gaussianity, and B -polarization. While these effects have been extensively studied, and a review of their impact can be found in Lewis & Challinor (2006), we are here concerned with the lensing due to strongly nonlinear objects such as galaxy clusters and smaller-scale structures. In particular, we focus our attention on the estimation of the small angular scale (high ℓ) correlations induced by this lensing. This marks a somewhat different direction to the extensive recent efforts to extend N-body simulation techniques to all-sky modelling (*e.g.* Fosalba *et al.* 2008; Das & Bode 2008; Carbone *et al.* 2008; Teyssier *et al.* 2009; Carbone *et al.* 2009).

N-body simulations are necessary to estimate some CMB anisotropies. This is the case for the gravitational anisotropies (weak lensing and Rees-Sciama effects) produced by strongly nonlinear cosmological structures. While simulations with sufficient resolution to model the formation of galaxies within an entire Hubble volume are currently out of reach, researchers are getting close to this goal (Kim *et al.* 2008; Teyssier *et al.* 2009). However, until such simulations are possible in order to estimate gravitational anisotropies in the CMB it is necessary to create an artificial periodic universe where copies of the simulation box at various redshifts are replicated back to a given redshift. While numerous alternatives exist for how this is achieved all the methods propagate CMB photons along appropriate directions within these model universes. When conducting this ray-tracing, box sizes, spatial scales and ray directions must be chosen in such a way that the periodicity of the artificial universe has no appreciable effects on the resulting anisotropy. The ray-tracing procedure used here achieves these goals and was described and applied in earlier papers,

where it was also compared with previous methods (Jain et al. 2000; White & Hu 2000). Two of these earlier papers dealt with weak lensing (Cerdá-Durán et al. 2004; Antón et al. 2005), and two others with the Rees-Sciama effect (Sáez et al. 2006; Puchades et al. 2006). The simulations discussed in these papers were conducted with the Particle-mesh (PM, *e.g.* Hockney & Eastwood 1988) N-body simulation algorithm. For the large simulation boxes required in our study (see below) the spatial resolution of PM simulations is moderate, at best. For this reason it was suggested in these papers that better N-body simulations might be necessary to estimate good CMB angular power spectra for large multipole indexes (ℓ values). This suggestion is confirmed in the present study, where AP3M (Adaptive Particle-Particle, Particle-Mesh; Couchman 1991) simulations with high resolution are performed to build up an appropriate periodic universe, in which the CMB photons are then moved according to the aforementioned ray-tracing procedure. A CMB angular power spectrum has been estimated from $\ell \sim 200$ to $\ell \sim 10000$, and the accuracy of this spectrum in various ℓ -intervals is discussed.

Motivated by a desire to match a number of cosmological constraints, including the five-year WMAP (Wilkinson microwave anisotropy probe) observations, high-redshift supernovae measurements and galaxy surveys, (*e.g.* Spergel *et al.* 2007; Vianna & Liddle 1996; Riess *et al.* 1998; Perlmutter *et al.* 1999) we consider a cosmological model in which the universe is flat and the initial fluctuation spectrum has an inflationary origin. It is assumed that only scalar perturbations are present and that weak lensing from gravitational waves is negligible. The resulting distribution of perturbations is then Gaussian and the perturbations themselves are purely adiabatic. Post inflation, the power spectrum of the perturbations is almost exactly of the Harrison-Zel’dovich (Harrison 1970; Zel’dovich 1970) form. This power spectrum is then modified during the radiation-dominated phase, as acoustic oscillations in the photon-baryon fluid damp growth, an effect accounted for by our use of a CMBFAST calculation of the transfer function. The following cosmological

parameters are used for consistency with the standard model (Komatsu et al. 2008; Hinshaw et al. 2008): (1) a reduced Hubble constant $h = 10^{-2}H_0 = 0.7$ (where H_0 is the Hubble constant in units of $\text{km s}^{-1} \text{Mpc}^{-1}$); (2) density parameters $\Omega_b = 0.046$, $\Omega_d = 0.233$, and $\Omega_\Lambda = 0.721$ for the baryonic, dark matter, and vacuum energy, respectively (the matter density parameter is then $\Omega_m = \Omega_b + \Omega_d = 0.279$); (3) an optical depth $\tau = 0.084$ which characterizes the reionization; and (4) a parameter $\sigma_8 = 0.817$ normalizing the power spectrum of the energy perturbations.

The layout of this paper is as follows: in Section 2 we outline salient issues in our map-making technique. We follow this in Section 3 with an outline of N-body methods and our ray-tracing technique. Results from our new simulations are presented in Section 4 along with a critical comparison to earlier work. We then compare our results to current observations and conclude with a brief discussion.

2. Map Construction

We begin by describing the procedure for constructing lensed maps of the CMB from small unlensed maps at the last scattering surface. Note that in this section and those following, we choose units such that $c = 8\pi G = 1$, where c is the speed of light and G the gravitational constant. For a quantity A , A_e and A_0 denote the value of A at, respectively, the time of emission (last scattering surface) and the present. The scale factor is $a(t)$, where t is the cosmological time, and its present value, a_0 , is assumed to be unity, which is always possible in flat universes. The unit vector \vec{n} defines the observation direction (line of sight).

Small, unlensed maps of CMB temperature contrasts ($\Delta = \delta T/T$) must be constructed to be subsequently deformed by lensing. These maps have been obtained with a method based on the fast Fourier transform (Sáez et al. 1996) and lead to small squared-Gaussian

maps of the contrast Δ . These maps are uniformly pixelised. The code designed to build up the unlensed maps (map making procedure), requires the CMB angular power spectrum, which has been obtained by running the CMBFAST code (Seljak & Zaldarriaga 1996) for the model described above. In order to deform the unlensed maps, the lens deviations corresponding to a set of directions, covering an appropriate region of the sky, must be calculated. These deviations are the quantities (Seljak 1996):

$$\vec{\delta} = -2 \int_{\lambda_e}^{\lambda_0} W(\lambda) \vec{\nabla}_{\perp} \phi \, d\lambda , \quad (1)$$

where $\vec{\nabla}_{\perp} \phi = -\vec{n} \wedge \vec{n} \wedge \vec{\nabla} \phi$ is the transverse gradient of the peculiar gravitational potential ϕ , and $W(\lambda) = (\lambda_e - \lambda)/\lambda_e$. The variable λ is

$$\lambda(a) = H_0^{-1} \int_a^1 \frac{db}{(\Omega_{m0}b + \Omega_{\Lambda}b^4)^{1/2}} . \quad (2)$$

In the case of weak lensing, the integral in Eq. (1) is usually integrated along straight paths, ignoring the small deflections associated with the lensing effect. This approximation, commonly known as the Born approximation, is equivalent to keeping first order terms in a positional expansion of the transverse potential as a function of the normal ray and its lensing offset. While this approximation is known to be comparatively inaccurate at small ℓ (*e.g.* Van Waerbeke *et al.* 2001), at $1000 \lesssim \ell \lesssim 10000$ detailed calculations using higher order perturbation theory suggest that corrections to the first order assumption are approximately two orders of magnitude lower than the first order term (Shapiro & Cooray 2006). Recent N-body simulation work examining the validity of the Born approximation (Hilbert *et al.* 2009) has shown corrections only begin to become significant at the 5% level for $\ell > 20000$. Since we are interested in calculating $1000 < \ell < 10000$ values we cautiously accept the errors inherent in the first order approach.

Once the deviations have been calculated, they can be easily used to get the lensed

maps from the unlensed ones. This is achieved using the relation

$$\Delta_L(\vec{n}) = \Delta_U(\vec{n} + \vec{\delta}) , \quad (3)$$

where Δ_L and Δ_U are the temperature contrasts of the lensed and unlensed maps, respectively.

Given the unlensed map Δ_U , and the map Δ_L obtained from it after deformation by lensing (the lensed map), the chosen power spectrum estimator can be used to get the quantities $C_\ell(U)$ and $C_\ell(L)$, whose differences $C_\ell(LU) = C_\ell(L) - C_\ell(U)$ can be considered as an appropriate measure of the weak lensing effect on the CMB. Moreover, a map of deformations $\Delta_D = \Delta_L - \Delta_U$ can be obtained and these can be analyzed to get another angular power spectrum $C_\ell(D)$. Since the maps L and U are not statistically independent, the spectra $C_\ell(D)$ and $C_\ell(LU)$ appear to be very different (see Antón et al. (2005) for details). Eight hundred unlensed maps are lensed (deformed) by using the same $\vec{\delta}$ field and the average $C_\ell(D)$ and $C_\ell(LU)$ spectra are calculated and analyzed. Both spectra are very distinct measures of the weak lensing effect under consideration. Many times, only the customary oscillating $C_\ell(LU)$ spectrum is shown; however, in a few appropriate cases, the $C_\ell(D)$ spectra are displayed. Our power spectrum estimator was described in detail in Arnau et al. (2002) and Burigana & Sáez (2003). Results obtained with this estimator were compared with those of the code ANAFast of the HEALPix (Górski et al. 1999) package in Arnau et al. (2002) and also in Puchades et al. (2006). These comparisons showed that our estimator is a very good one in the case of regularly pixelised squared maps as analyzed here.

3. N-body simulations and ray-tracing procedure

3.1. N-body simulation technique

The primary simulations presented in this work were run using a parallel OpenMP-based implementation of the “HYDRA” code (Thacker & Couchman 2006). This code uses the AP3M algorithm to calculate gravitational forces within a simulation containing N_p particles. In the AP3M algorithm a cubic “base” mesh of size N_c cells per side is supplemented by a series of refined-mesh P3M calculations to provide sub-mesh resolution. Gravitational softening is implemented using the S2 softening kernel (Hockney & Eastwood 1988) which is remarkably similar in shape to the cubic spline softening kernel used in many treecodes (*e.g.* Hernquist & Katz 1989). The S2 softening used in the kernel is $2.34 \times S_p$ where S_p is an equivalent Plummer softening length which we quote throughout the paper to enable a simple comparison to other work. The softening length is held constant in physical coordinates subject to the resolution not falling below 0.6 of the interparticle spacing at high redshift. This technique is widely applied (*e.g.* Springel *et al.* 2005) and is a compromise between assuring that the potential energy of clusters does not evolve significantly at low redshift, while still ensuring structures and linear perturbations at high redshift are followed with reasonable accuracy.

Initial conditions were calculated using the standard Zel’dovich approximation technique (Efstathiou *et al.* 1985), and all simulations were started at a redshift of $z = 50$, which is sufficiently early to place modes in the linear regime. To account for the impact of varying box sizes, L_{box} , we considered simulations of size $256h^{-1}$ Mpc, $512h^{-1}$ Mpc, and $1024h^{-1}$ Mpc and a full list of N-body simulation and ray-tracing parameters is given in Table 1. At $z = 6$ (the beginning of our ray-tracing epoch in the simulation), the box sizes of $256h^{-1}$ Mpc, $512h^{-1}$ Mpc, and $1024h^{-1}$ Mpc correspond to square sky patches with angular sizes, Φ_{map} , of 2.48° , 4.96° , and 9.92° , respectively. These are then the sizes of our

Table 1. Lensing Simulations

Name	Algorithm	L_{box} $/h^{-1} Mpc$	Mode set	N_p	M_p $10^{10} M_\odot$	N_c	S_p $/h^{-1} kpc$	N_{dir}	z_{in}	Δ_{ps} $/h^{-1} kpc$	Δ_{ang} ,	Direction
RLS_AA	AP3M	512	A	512^3	11	1024	12	512	6	25	0.59	D512A
RLS_AB	AP3M	512	A	512^3	11	1024	12	512	6	25	0.59	D512B
RLS_BA	AP3M	512	B	512^3	11	1024	12	512	6	25	0.59	D512A
RLS_CA	AP3M	512	C	512^3	11	1024	12	512	6	25	0.59	D512A
LS_LDA	AP3M	1024	D	512^3	88	1024	24	1024	6	50	0.59	D1024A
LS_MAB	AP3M	512	A	256^3	88	512	24	512	6	50	0.59	D512B
LS_ΔS1AA	AP3M	512	A	512^3	11	1024	24	512	6	50	0.59	D512A
LS_ΔS2AA	AP3M	512	A	512^3	11	1024	36	512	6	75	0.59	D512A
LS_Δ1AA	AP3M	512	A	512^3	11	1024	12	512	6	12	0.59	D512A
LS_Δ1AB	AP3M	512	A	512^3	11	1024	12	512	6	12	0.59	D512B
LS_Δ1BA	AP3M	512	B	512^3	11	1024	12	512	6	12	0.59	D512A
LS_Δ1BB	AP3M	512	B	512^3	11	1024	12	512	6	12	0.59	D512B
LS_Δ2AA	AP3M	512	A	512^3	11	1024	12	512	6	40	0.59	D512A
LS_Δ2AB	AP3M	512	A	512^3	11	1024	12	512	6	40	0.59	D512B
LS_Δ2BA	AP3M	512	B	512^3	11	1024	12	512	6	40	0.59	D512A
LS_Δ2BB	AP3M	512	B	512^3	11	1024	12	512	6	40	0.59	D512B
LS_HEA	AP3M	256	E	512^3	1.4	1024	6	512	6	15	0.29	D256A
LS_MGA	AP3M	512	G	256^3	88	512	24	512	6	60	0.59	D512A
LS_LHA	AP3M	512	H	128^3	704	256	48	512	6	120	0.59	D512A
PMLS	PM	256	F	512^3	1.4	512	1000	256	6	500	0.59	D256A

Note. — List of the parameters used in the lensing simulations. Columns three to eight give information associated with the N-body simulations, namely the box size, L_{box} , the set of initial modes (determined by the box size and a single random seed), the number of particles used, N_p , the mass of the individual particles, M_p , the number of Fourier cells along each side of the simulation, N_c , and the Plummer softening length used, S_p . All N-body simulations were started at a redshift of $z = 50$. The following five columns give parameters associated with the lensing calculation, namely the number of rays along the edge of the map, N_{dir} , the initial redshift at which ray tracing begins, z_{in} , the distance between evaluations on the geodesic Δ_{ps} , the angular resolution of the CMB lensed maps Δ_{ang} , and the preferred direction used (see Table 2).

constructed CMB maps for each simulation.

3.2. Ray-tracing technique

3.2.1. Lensing regimes

As in our previous work (Antón et al. 2005) we divide the total lensing effect into three parts:

- AWL (A weak lensing), namely the effect due to scales $k > 2\pi/L_{max}$ (where $L_{max} = 42h^{-1}$ Mpc) at redshifts $z < 6$. This signal is dominated by strongly nonlinear scales
- BWL, the lensing signal due to scales $k < 2\pi/L_{max}$ which corresponds to modes that are always in the linear regime down to $z = 0$
- CWL, the lensing signal due to scales $k \geq 2\pi/L_{max}$ but at redshifts $z > 6$

The goal of this paper is to calculate the AWL signal, using ray-tracing through N-body simulations, to ℓ values in the range 1000 – 10000. Since the modes associated with the BWL component are specifically chosen to correspond to scales that are linear down to $z = 0$, which is set by wavenumbers $k \lesssim 0.15h$ Mpc $^{-1}$ (Smith *et al.* 2003), the BWL component can be calculated with the linear approach implemented in CMBFAST. The CWL component involves modes in the mildly nonlinear regime which can, nonetheless, be evolved via approximation schemes (Zel’dovich 1970; Sandarin & Zel’dovich 1989; Moutarde et al. 1991). Standard semi-analytical methods designed to study weak lensing in the nonlinear regime should also apply in this case, hence, the CWL effect can be calculated without resorting to N-body techniques. This calculation can be performed using the nonlinear version of CMBFAST which is based on semi-analytical approaches

(Lewis & Challinor 2006). For these reasons we begin ray tracing within the simulation at $z = 6$ and consider nonlinear spatial scales having wavenumbers $k \geq 2\pi/L_{max}$. Other methods utilizing simulations have also included the contribution to lensing from all scales above a certain redshift using special techniques (Das & Bode 2008; Carbone *et al.* 2008).

In Figure 1 we show calculations of the LU angular power spectra for the AWL, BWL and CWL lensing regimes for $3200 < \ell < 10000$ using the nonlinear lensing implementation in CMBFAST. Note that for $\ell < 3500$ the AWL and CWL effects are too small to be calculated with CMBFAST due to the fact that these spectra are obtained as differences between other spectra provided by the code. Both the AWL and CWL effects, as calculated by CMBFAST, are clearly small with the CWL effect being virtually negligible in the $3200 < \ell < 10000$ range. As anticipated, the BWL effect is dominant. The calculation of the AWL effect provides an initial estimate of the signal we wish to calculate with the simulation. We have verified that, for $\ell < 10000$, the BWL effects calculated by using both the linear and nonlinear methods implemented in CMBFAST are almost identical, which proves that the BWL component is linear, as expected.

3.2.2. Calculation of the lens deviation integral

An estimate of the lens deviation integral, given in Eq. (1), is computed via a numerical integration performed along the background null geodesics from the comoving distance $D_{max} \simeq 5900h^{-1} \text{ Mpc}$ corresponding to $z = 6$ (in the model under consideration) to the observer position. The gradient of the peculiar potential $\vec{\nabla}\phi$ used in the integrand of Eq. (1) is obtained from the simulation but is not exactly the same as that used within the N-body calculation. Instead, the gradient is found by subtracting the part of the full N-body potential produced by linear spatial scales larger than $42h^{-1} \text{ Mpc}$.

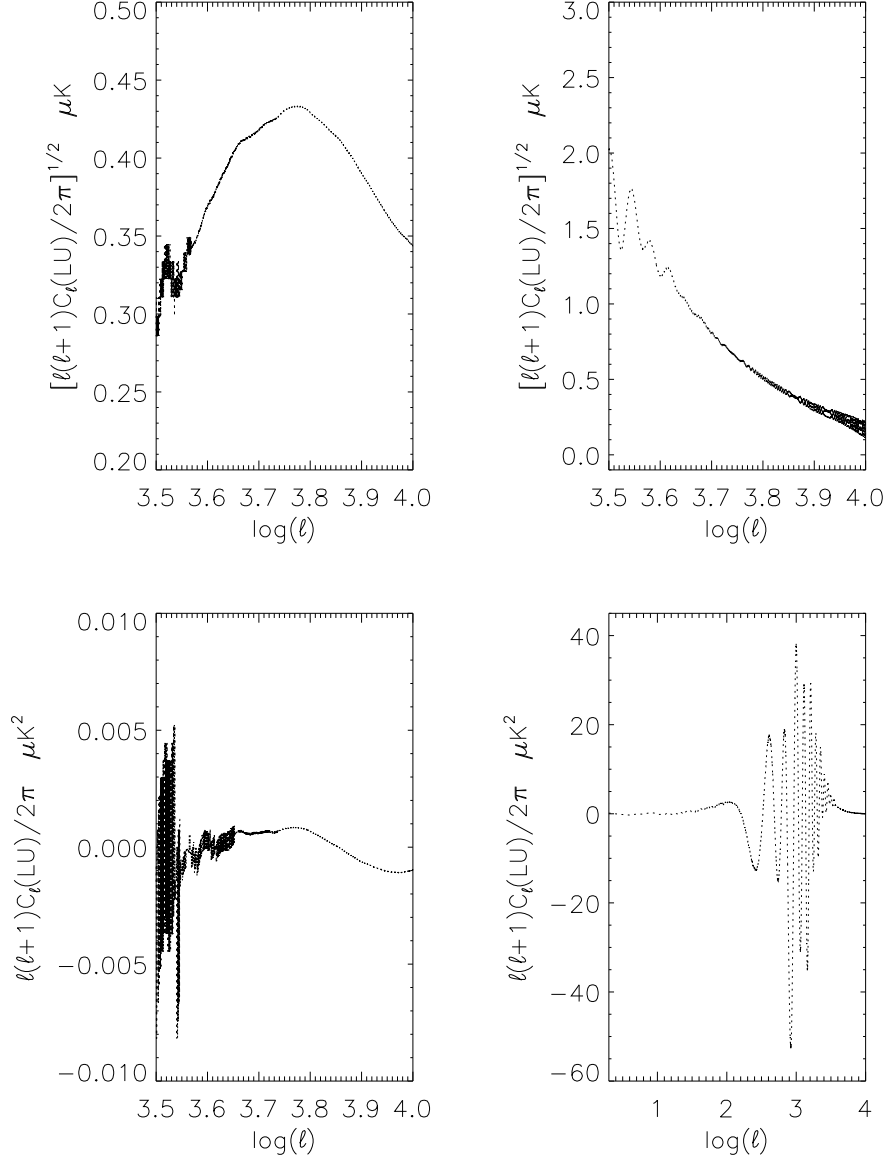


Fig. 1.— Results from CMBFAST calculations. Top-left, top-right and bottom left panels exhibits the LU angular power spectrum for $\ell > 3200$ in the cases AWL, BWL, and CWL, respectively. Bottom-right panel is the LU spectrum corresponding to the BWL effect for $\ell < 10000$. This effect dominates against AWL and CWL for $\ell < 3000$.

Specifically, our algorithm for determining the potential gradient, which is proportional to the force, is as follows:

1. Decide upon the direction of the normal rays representing the geodesics (see Section 3.2.3)
2. Assuming the Born approximation and using the photon step distance Δ_{ps} (see Section 3.2.3) determine all the evaluation positions and times on the geodesics within the simulation volume from $z = 6$ down to the final redshift
3. Associate test particles with each of these positions and times
4. At each time-step of the N-body simulation (while it is running) determine which test particles require force evaluations
5. At each test particle position evaluate the force on the test particle using the long-range FFT component and short-range PP correction as in the HYDRA algorithm
6. During the FFT convolution for the test particles eliminate contributions from scales larger than $42h^{-1}$ Mpc by removing the signal from wavenumbers satisfying $k \lesssim 0.15h$ Mpc $^{-1}$
7. If the evaluation time for a point on the geodesic lies between two time-steps calculate a linear interpolation of the two forces from the time-steps that straddle the correct time
8. Resolve the force into its transverse component and hence recover the transverse component of the potential gradient

Once all the potential gradients are evaluated we can calculate the lensing deviation integrals. We emphasize that our algorithm ensures the potential gradient along normal rays is calculated very accurately and corresponds exactly (modulo the removal of power from scales greater than $42h^{-1}$ Mpc) to that in the simulation. We do not resort to smoothing

onto grids or the creation of lensing planes “on the fly”. The main drawback of our method is that since lensing is now an integral part of the N-body simulation, a different preferred direction requires a new N-body simulation.

3.2.3. *Photon propagation paths*

To calculate the photon propagation, the CMB photons are moved through the simulation volume along specially chosen paths to avoid repeatedly sampling the same structures. This approach uses all steps from the simulation and by using the periodicity of the box volume there are no discontinuities in the matter field anywhere. In principle this approach is similar to tiling methods that are used elsewhere (*e.g.* White & Hu 2000; Hamana *et al.* 2001; Sato *et al.* 2009). These methods are based on independent PM simulations with decreasing sizes that telescope in resolution along the line of sight. In our “tiling” the matter field is constantly being updated by the AP3M code as the time-step changes and, consequently, it is not limited by the box size. We also take care to ensure paths are taken which avoid, as much as possible, periodicity effects. This is notably different from other approaches using random translations and orientations (*e.g.* Carbone *et al.* 2008) of the simulation volume which, unavoidably, have discontinuities at adjoining radial shells. While the signal from such discontinuities is likely small, our method has the advantage of avoiding it completely.

Choosing the directions for the ray propagation is not entirely trivial. For the directions parallel to the box edges, periodicity effects are clearly very strong. Photons moving along these directions would pass close to the same structures in successive boxes and, consequently, the lensing effect of the same structure would be included a number of times (one per crossed box). This repetition would lead to a false magnification of lens deviations. However, as has been emphasized in Antón *et al.* (2005) and Sáez *et al.* (2006), periodicity

effects are negligible along certain directions, hereafter called *preferred directions*.

In order to define preferred directions, it can be assumed that: (i) the x , y , and z axes are parallel to the box edges; (ii) the angles θ and φ are spherical coordinates defined with respect to these axes; (iii) photons moving along the direction \vec{n} , cross the (y, z) face of a box at point P , and the next (y, z) face at point Q ; and (iv) if the segment PQ is projected onto the (y, z) plane, the length of the resulting projection is ζ_{PQ} . Then, if the condition $\zeta_{PQ} > L_{max}$ is satisfied, the direction \vec{n} is assumed to be a preferred one. Taking into account this definition of preferred directions and the cutoff performed at the scale L_{max} , it is clear that photons moving along preferred directions enter successive boxes through independent uncorrelated regions. Moreover, for these directions and the box sizes of interest, it can be easily verified that the CMB photons can travel from $z = 6$ to $z = 0$ ($\sim 5900h^{-1} \text{ Mpc}$) through different uncorrelated regions (without repetitions) located in successive simulation boxes. Periodicity effects can, therefore, be assumed to be negligible. The total number of crossed boxes is denoted by N_{cr} .

Some preferred directions used in this paper are defined in Table 2, where the first column gives the names of all these directions. Each of them has been used in universes covered by simulation boxes with a given size, as detailed in the second column. The third and fourth columns show, respectively, the angles θ and φ (spherical coordinates) defining the corresponding direction. The distance ζ_{PQ} defined in the previous paragraph is given in the fifth column and, finally, in the last column the number of boxes crossed by the CMB photons from redshift $z = 6$ to the present is given. From the values of Table 2, it is clear that the distance ζ_{PQ} is much greater than $L_{max} = 42h^{-1} \text{ Mpc}$ in all four cases, which ensures that other directions close enough to the listed ones are also preferred directions.

Table 2. Preferred directions for ray tracing.

Direction	L_{box}	θ	φ	ζ_{PQ}	N_{cr}
D256A	256	76.76	11.31	79.98	22.00
D512A	512	76.76	11.31	159.95	11.00
D512B	512	68.43	18.435	273.20	10.17
D1024A	1024	59.19	26.57	853.33	4.43

Note. — Distances L_{box} and ζ_{PQ} are given in units of $h^{-1} \text{ Mpc}$, and the spherical coordinates θ and φ in degrees

We proceed as follows: any direction of Table 2 is assumed to point toward the center of a squared map, whose angular size corresponds to the box size appearing in the second column (as noted above). Then, these squared maps are uniformly pixelised by choosing a certain number of pixels, N_{pix} , per edge. The angular resolution is then $\Delta_{ang} = \Phi_{map}/N_{pix}$. The directions of all the pixels are preferred ones and, consequently, lens deviations can be calculated for each pixel—with no significant periodic effects—across the full map.

The parameters involved in the ray-tracing procedure are thus summarized: a number of directions, N_{dir} , per edge of the squared CMB map (one per pixel, $N_{dir} = N_{pix}$); an initial redshift, z_{in} , for the calculation of lens deviations; a step, Δ_{ps} , to perform the integral in Eq.(1) (hereafter called the photon step); and the angles θ and φ defining the preferred direction.

Hereafter, a lensing simulation (LS) is the calculation of the $\vec{\delta}$ -deviations along the pixel directions, plus the construction of the Δ_U , Δ_L , Δ_D maps and the estimation of $C_\ell(D)$ and $C_\ell(LU)$ (angular power spectra). An LS is characterized by the parameters and initial conditions required by the N-body simulation together with the parameters of the ray-tracing procedure. The lensing simulations (LSs) obtained from the parameters: $L_{box} = 512h^{-1} \text{ Mpc}$, $N_p = 512^3$, $N_c = 1024$, $S_p = 12h^{-1} \text{ kpc}$, $N_{dir} = 512$, $z_{in} = 6$ (as in all the simulations used in the paper), and $\Delta_{ps} = 25h^{-1} \text{ kpc}$, are hereafter called reference lensing simulations (RLSs). The angular resolution of these simulations is $\Delta_{ang} \simeq 0.59'$ ($\ell \simeq 18,600$). There are an infinite number of possible realizations of this type of LSs corresponding to different initial conditions for the N-body simulation as well as to distinct preferred directions. We also consider the effect on the LSs of changing parameters to ensure that the calculation of the power spectra $C_\ell(D)$ and $C_\ell(LU)$ is as robust and accurate as possible.

4. Results

4.1. Effect of changing the final ray-tracing redshift

To determine the impact of changing the final ray-tracing epoch, the RLS_AA lensing simulation (based on the preferred direction *D512A*, see tables 2 & 1), was used to estimate lensing from $z_{in} = 6$ to final redshifts between 0.5 and 0. Results are shown in Fig. 2, where the D angular power spectra corresponding to the final redshifts 0.3 (dotted line), 0.2 (solid line), and 0.0 (dashed line) are presented. Clearly, these three spectra are very similar. We find the same result for the LU spectra (these results are omitted since the addition of five oscillating lines would lead to a confusing plot and add little information). Based upon these results we conclude that the signal produced between redshifts 0.2 and 0 contributes negligibly to the total lensing. Given this fact, and that the CPU time required to evolve between $z = 0.2$ and $z = 0$ is comparatively lengthy for our code (due to the absence of individual particle time-steps), our calculations are performed between redshifts $z_{in} = 6$ and $z_{end} = 0.2$. The same study has been done for other RLSs corresponding to different initial conditions and preferred directions. The conclusions are the same in all the cases, namely a negligible effect between $z = 0.2$ and $z = 0$. We note that this conclusion is in close agreement with that of Carbone *et al.* (2008) who showed that stopping at $z = 0.22$ produced a deficit in the low ℓ signal but a negligible difference for $\ell > 350$.

4.2. AP3M simulations contrasted to PM

We next compare LSs constructed from PM and AP3M N-body codes to examine the impact of sub-mesh-scale resolution on the lensing signal. In Fig. 3 we plot the $C_\ell(LU)$ (top panel) and $C_\ell(D)$ (bottom panel) for RLS_BA (solid line) along with the same spectra for PMLS (dashed line), obtained from a PM code. Details of the PM code can be found

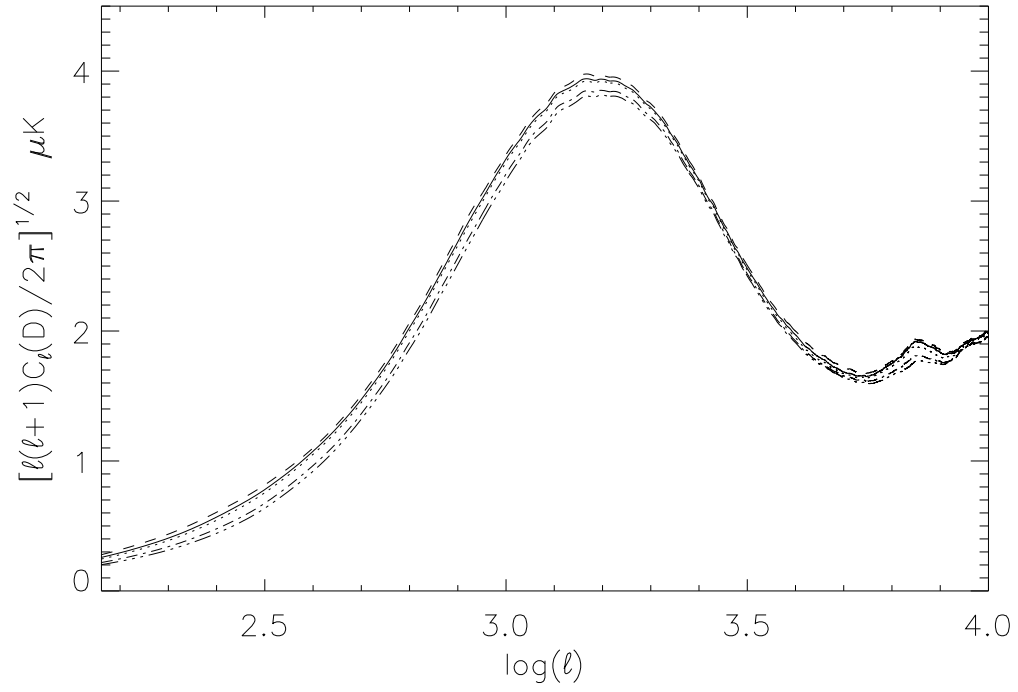


Fig. 2.— D angular power spectra corresponding to RLS-AA at different final redshifts. Curves corresponding to z_{end} values of 0.5 (triple-dot-dash), 0.4 (dot-dash), 0.3 (dots), 0.2 (solid), and 0.0 (dashes) are shown.

in Quilis et al. (1998); this code has been used in previous papers (*e.g.* Antón et al. 2005). We emphasize that the same ray-tracing procedure, described in Section 3, is used in both codes. The parameters of the PMLS (see Table 1) are as follows: $L_{box} = 256h^{-1} \text{ Mpc}$, $N_p = 512^3$, $N_c = 512$, $N_{dir} = 256$, and $\Delta_{ps} = 0.5h^{-1} \text{ Mpc}$, and the preferred direction is D256A (see Table 2). The effective resolution E_{res} of the PM code is two cells ($1 h^{-1} \text{ Mpc}$ in this case); hence, in the PMLS, the photon step Δ_{ps} must be smaller than $1h^{-1} \text{ Mpc}$ to take advantage of the PMLS resolution. It has been verified that $\Delta_{ps} = 0.5h^{-1} \text{ Mpc}$ (half of E_{res}) is a good value for the photon step (smaller values lead to very similar results). In keeping with other N-body work (*e.g.* Moore *et al.* 1998), the true effective resolution of the AP3M simulations is estimated to be $E_{res} \sim 5S_p$, which means that, in our RLSs, the photon step is a little smaller than a half of the effective resolution.

Examination of Fig. 3 shows that the PMLS traces the peaks, but the amplitudes are too small and, moreover, the $C_\ell(LU)$ quantities quickly tend to zero as ℓ increases. However, in the AP3M case, the peaks have greater amplitudes and, furthermore, a signal of a few micro-Kelvin appears for high ℓ values. Similar conclusions follow from the D spectra of the bottom panel, which can be directly compared with Antón et al. (2005), where this kind of spectrum was used. These results show that the PMLS underestimates the lensing signal we are calculating. Hence, high resolution N-body simulations, be they AP3M or computed using some alternative algorithm, are necessary to estimate CMB weak lensing from strongly nonlinear structures.

4.3. Variance of power spectra due to modes in the initial conditions

Having shown that the results from the AP3M simulations are distinctly different from those of the PM simulations, we must still account for variability of results due to changing the random modes in the initial conditions of the simulation. To this end we show, in

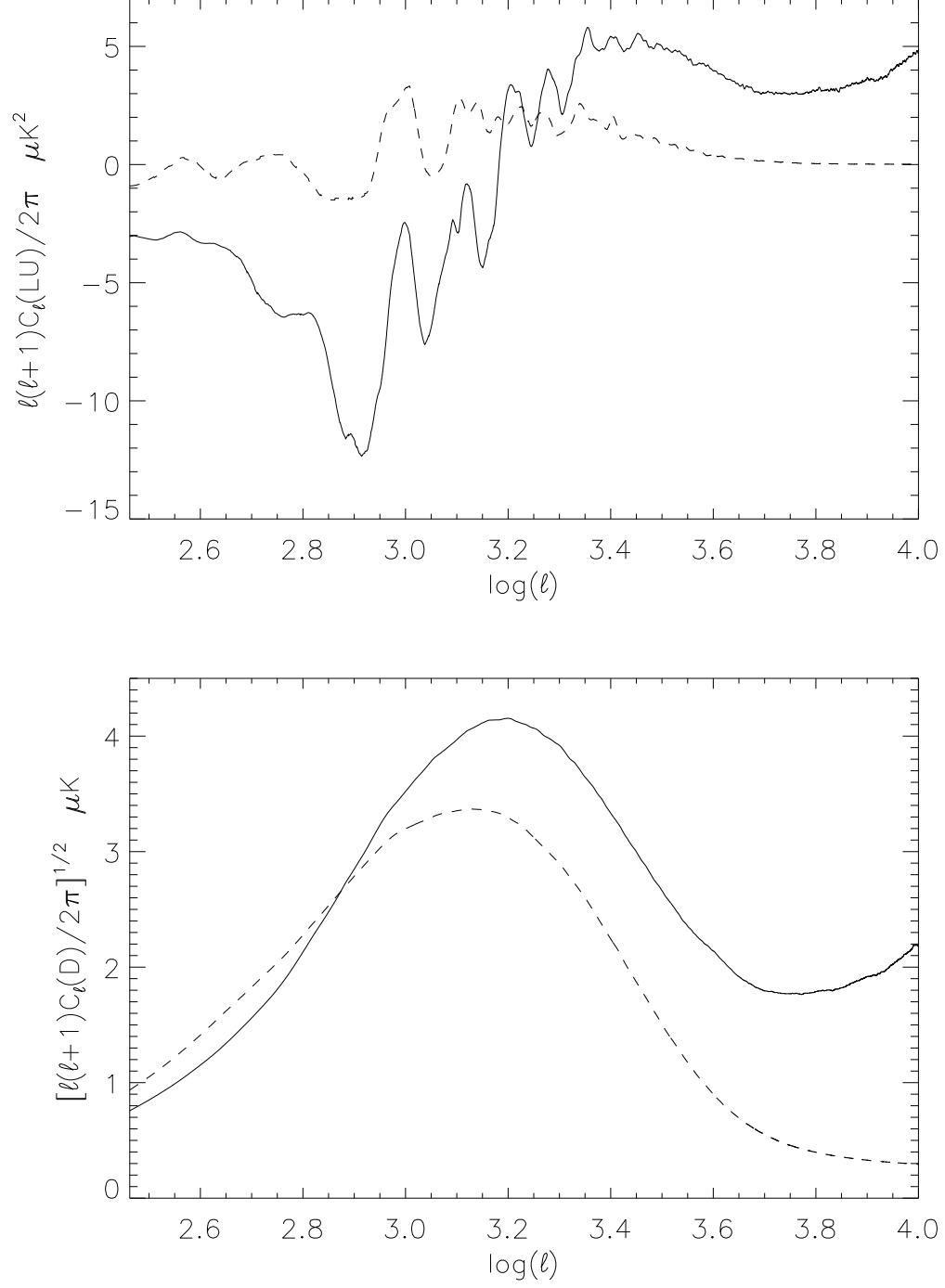


Fig. 3.— Top: LU angular power spectra corresponding to the RLS_BA (solid line) LS, and to the PMLS LS defined in the text (dashed line). Bottom: D spectra for the same simulations as in top panel.

the top panel of Fig. 4, the LU angular power spectra corresponding to three distinct RLSs, namely, RLS_AA, RLS_BA & RLS_CA, each drawn from a different realization of the modes but using the same preferred direction ($D512A$ in Table 2). The results are clearly qualitatively very similar and the only noticeable quantitative differences are below $\ell \sim 1000$. This is not entirely surprising since the lower the ℓ value the larger the sample variance (Knox 1995; Scott et al. 1994). Additionally, the largest deviation occurs at the point where the signal is weakest, again an unsurprising result.

These results suggest that a good average LU spectrum can be achieved from just a few chosen RLSs simulations, perhaps as few as two. We have verified this assertion in the bottom panel of Fig. 4, by plotting the average of two of the RLSs as compared to the average of all three RLSs. Both average spectra are so similar that only two RLSs suffice to get a very good average LU spectrum in the ℓ -interval under consideration. Unsurprisingly, the average signals for $\ell < 1000$ are in good agreement, as would be expected if the differences in the single realizations were due to sample variance. For $\ell > 1000$, the spectra of the different realizations are so similar that a unique RLS leads to a rather good LU spectrum of the lensing effect under consideration ($L < L_{max}$ and $z < z_{in} = 6$).

We emphasize that the sample variance we have been talking about is inherent in the lensing calculation itself, rather than the CMB maps themselves. For each RLS, the spectra are calculated from 800 small maps having a size of 4.96 degrees; which is a necessary step to understand small sample variances (small deviations from spectrum to spectrum).

4.4. Variance of power spectra due to different preferred directions

In terms of the variance produced by different preferred directions, the ergodic nature of the ray-tracing means that we might reasonably expect the same level of variance seen

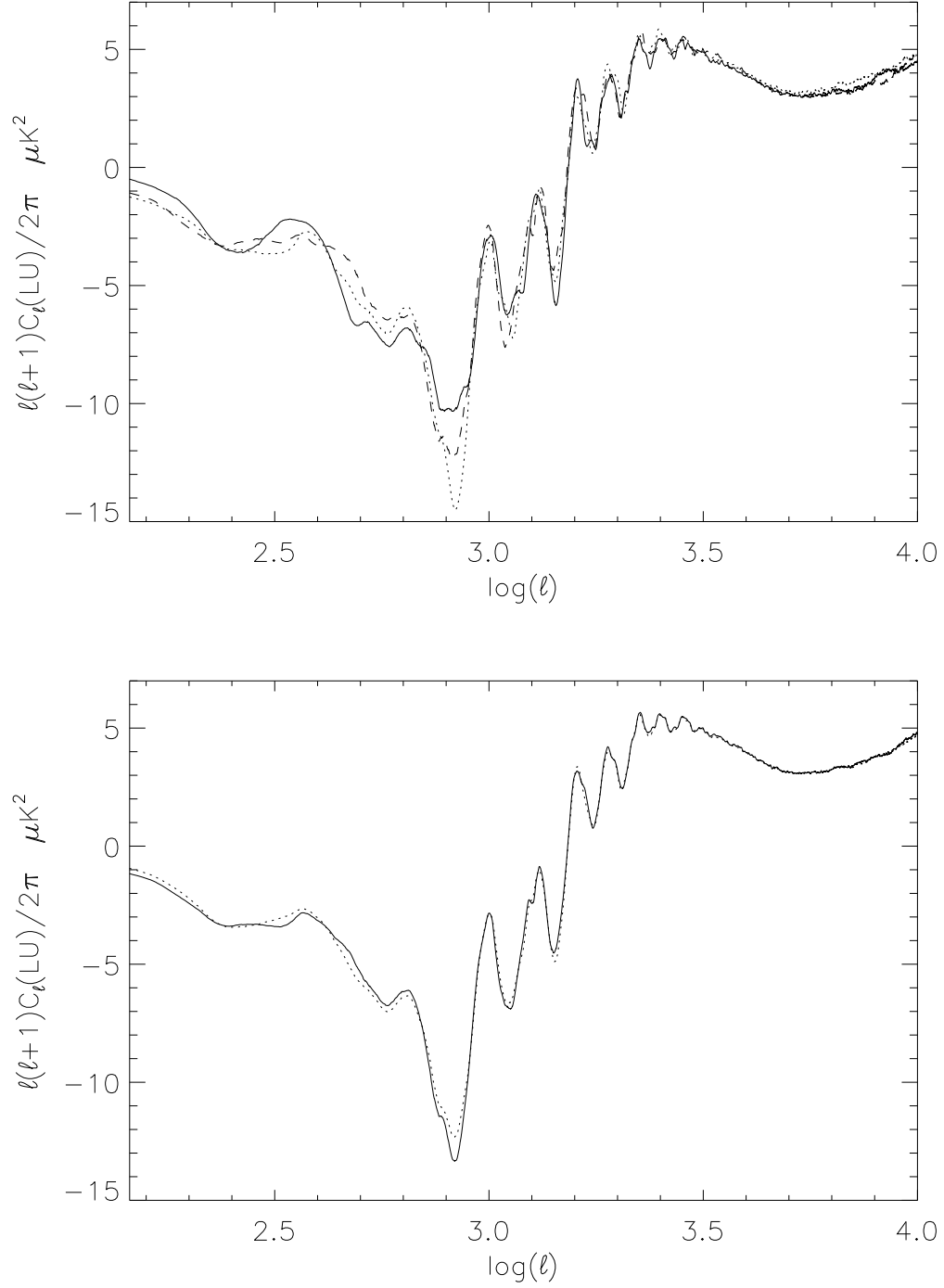


Fig. 4.— Top: Three LU angular power spectra extracted from distinct RLSs, namely RLS_AA (solid), RLS_BA (dashed), RLS_CA (dotted). Bottom: the dotted line gives the average LU spectrum of the three RLSs of the top panel, whereas the solid line corresponds to the average of two spectra, namely just RLS_BA and RLS_CA.

for the different N-body realizations with differing modes. Nevertheless, choosing a different preferred direction for a given RLS means that the photons move through different regions of the simulation box and cross box faces in different places and a different number of times. So the trajectories are not fully equivalent, in turn producing lensing deviations that are subtly distinct. To evaluate this difference we plot, in Fig. 5, two LU angular power spectra for the RLSs RLS_AA and RLS_AB which use the same initial modes, but have preferred directions D512A and D512B. The similarity of the two curves indicates that, as anticipated, results are almost independent of the chosen preferred direction, and that our ray-tracing procedure is robust.

4.5. Impact of simulation box size on the power spectra

Thus far we have considered AP3M simulations with box sizes $L_{box} = 512h^{-1}$ Mpc, and hence the LU and D spectra have been obtained from small maps of angular size $\Phi_{map} = 4.96^\circ$. We next examine whether these values are too small to make robust predictions.

In order to answer this question, we conducted an LS, labeled LS_LDA in Table 1, with $L_{box} = 1024h^{-1}$ Mpc and $N_{dir} = 1024$, which leads to a lensed map of size $\Phi_{map} = 9.92^\circ$ and with the same angular resolution as in the RLSs. Since simulating a larger volume at fixed particle resolution requires a larger softening and the corresponding photon step, the values $S_p = 24h^{-1}$ kpc, and $\Delta_{ps} = 60h^{-1}$ kpc were used. The preferred direction was D1024A (see Table 2). To compare to this simulation we also ran another LS, denoted LS_MAB, with parameters set to mimic the LS_LDA simulation but in 1/8th the volume and using 1/8th the number of particles. The LU spectra obtained for the two simulations are shown in Fig. 6, and are extremely similar. This is despite the fact that these two simulations have differing initial conditions, different box sizes, and different numbers of crossed boxes,

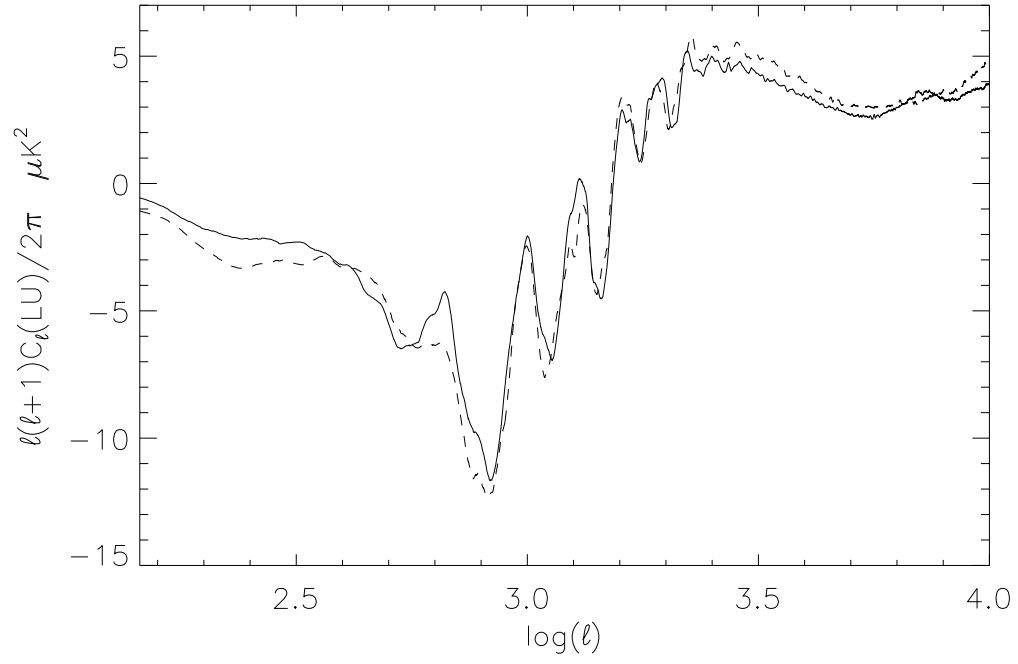


Fig. 5.— LU angular power spectra obtained from RLS_AA and RLS_AB which share the same N-body initial conditions but have distinct preferred directions. The dashed (solid) line corresponds to RLS_AA (RLS_AB) and hence the direction D512A (D512B).

N_{cr} . Hence we conclude that a box size of $512h^{-1} \text{ Mpc}$ —the same as that of the RLSs—is large enough to get very good angular power spectra for the range of ℓ considered. Even smaller sizes, *e.g.*, $256h^{-1} \text{ Mpc}$, can be used when only large enough ℓ values are under consideration (see below).

4.6. Noise in the power spectra

Although we do not directly calculate the 2d lensing potential or convergence we can examine the power spectrum of the angle $\alpha = |\vec{\delta}|$ as in Carbone *et al.* (2008). At our final redshift of 0.2, the angular resolution of our RLSs ($0.59'$) corresponds to a comoving separation of $100h^{-1} \text{ kpc}$, which is still larger than our nominal N-body resolution of $5S_p = 60h^{-1} \text{ kpc}$. Since this is the effective resolution in the ray-tracing we do not need to worry about the intrinsic resolution of our maps falling below that of the N-body simulation.

In Fig. 7 we plot the power spectrum of the lens deviations in the interval $2000 < \ell < 10000$. We have quantified the noise in this signal by considering box sizes of $1024h^{-1} \text{ Mpc}$, $512h^{-1} \text{ Mpc}$, $256h^{-1} \text{ Mpc}$ although our smallest box has an effective angular resolution that is twice as small as the other two simulations. For comparison to semi-analytic methods we also include the *total* lensing signal predicted by CAMB in this ℓ range. Comparing to a running average constructed by binning the average signal in $\ell \pm 100$, the RMS deviations relative to the overall signal are 4.1%, 5.3% and 6.2% for the three box sizes, respectively. Although we do see an increase in the relative noise with reducing box size, the overall noise is much less than the underlying signal. Further, the absolute value of the signals are in close agreement as well, the largest difference being $\sim 15\%$ at $\ell = 2000$ and the qualitative shape of the power spectra agree well at least for $\ell < 7000$. For $\ell = 10000$ we see a difference of 50% in the signals, and we are not confident of convergence in the interval $7000 < \ell < 10000$ (see Sections 4.8, 4.9 for an extensive

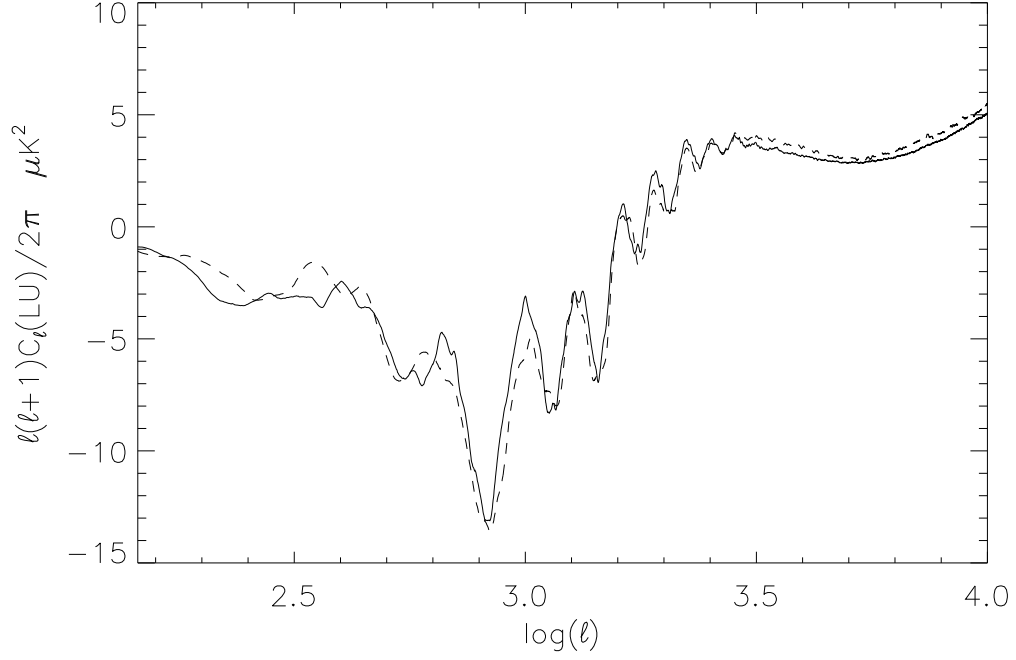


Fig. 6.— LU angular power spectra extracted from two LS simulations (LS_LDA, solid line and LS_MAB, dashed line) that differ in box sizes but use similar effective particle and map resolutions. The simulations share the same softening and photon steps, namely $S_p = 24h^{-1} \text{ kpc}$ and $\Delta_{ps} = 60h^{-1} \text{ kpc}$, but for the LS_LDA LS $L_{box} = 1024h^{-1} \text{ Mpc}$, $N_p = 512^3$ while for the LS_MAB LS, $L_{box} = 512h^{-1} \text{ Mpc}$, $N_p = 256^3$. The initial conditions of these LSs are fully independent and different preferred directions are used.

discussion of convergence issues).

4.7. Impact of spatial resolution

Having examined sampling issues related to box sizes and preferred directions we now address the impact of force softening and the step size in the ray-tracing. As a first investigation, we varied parameters S_p and Δ_{ps} , in lock-step with the remaining RLS parameters held fixed. A ratio $E_{res}/\Delta_{ps} \simeq 2.5$, identical to that of the RLS simulations has been assumed in all the cases, thus maintaining a constant ratio between the photon step and the effective resolution (*i.e.* 2.5 photon steps per effective resolution interval). We considered the following new pairs of S_p and Δ_{ps} : (i) $S_p = 24h^{-1} \text{ kpc}$ and $\Delta_{ps} = 50h^{-1} \text{ kpc}$ and, (ii) $S_p = 36h^{-1} \text{ kpc}$ and $\Delta_{ps} = 75h^{-1} \text{ kpc}$, and call the LSs associated with these parameters LS_ΔS1AA and LS_ΔS2AA respectively. The $C_\ell(LU)$ for these LSs, along with RLS_BA for comparison, are given in Fig. 8. Up to $\ell \sim 7000$ the three spectra are very similar, although for $\ell > 7000$ we see a small separation in the results. For $\ell > 5000$, the trend with decreasing softening and photon-step appears to be systematic, a smaller softening leading to smaller $C_\ell(LU)$ coefficients. Nevertheless, a smaller softening does not necessarily mean a more realistic simulation and, consequently, we cannot decide which of the three lines of Fig. 8 is closer to the true spectrum. Regardless of this issue, any of these lines gives a good estimate of the required spectrum for $\ell < 7000$.

To address the role of the photon step alone, we next held fixed all the RLS parameters except the photon step, Δ_{ps} . Along with our original choice of $\Delta_{ps} = 25h^{-1} \text{ kpc}$, two new values were considered: $\Delta_{ps} = 12h^{-1} \text{ kpc}$ ($\sim E_{res}/5$, corresponding to LSs LS_Δ1AA, LS_Δ1AB, LS_Δ1BA, LS_Δ1BB), and $\Delta_{ps} = 40h^{-1} \text{ kpc}$ (a little smaller than $\sim E_{res}$, corresponding to LSs LS_Δ2AA, LS_Δ2AB, LS_Δ2BA, LS_Δ2BB). For each of the Δ_{ps} two distinct preferred directions, namely $D512A$ and $D512B$, were considered along with two

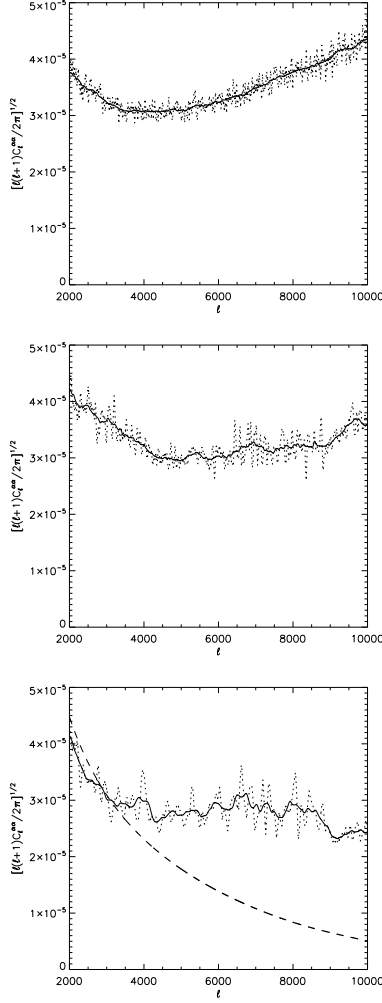


Fig. 7.— Top, medium and bottom panels correspond to box sizes of $1024h^{-1}$ Mpc (LS_LDA), $512h^{-1}$ Mpc (RLS_BA), and $256h^{-1}$ Mpc (LS_HEA). Dotted lines correspond to the correlations extracted from the simulated α maps. Solid lines are averaged spectra in running bins of size $\ell \pm 100$. The mean amplitude and the *rms* of the relative errors (dotted-solid/solid) are $(-0.00072, 0.041)$, $(-0.00065, 0.053)$, and $(-0.00056, 0.062)$ in the top, medium, and bottom panels, respectively. The dashed line in the bottom panel corresponds to the total lensing signal predicted by CAMB. Note that the solid and dotted lines in all panels correspond to the AWL lensing component.

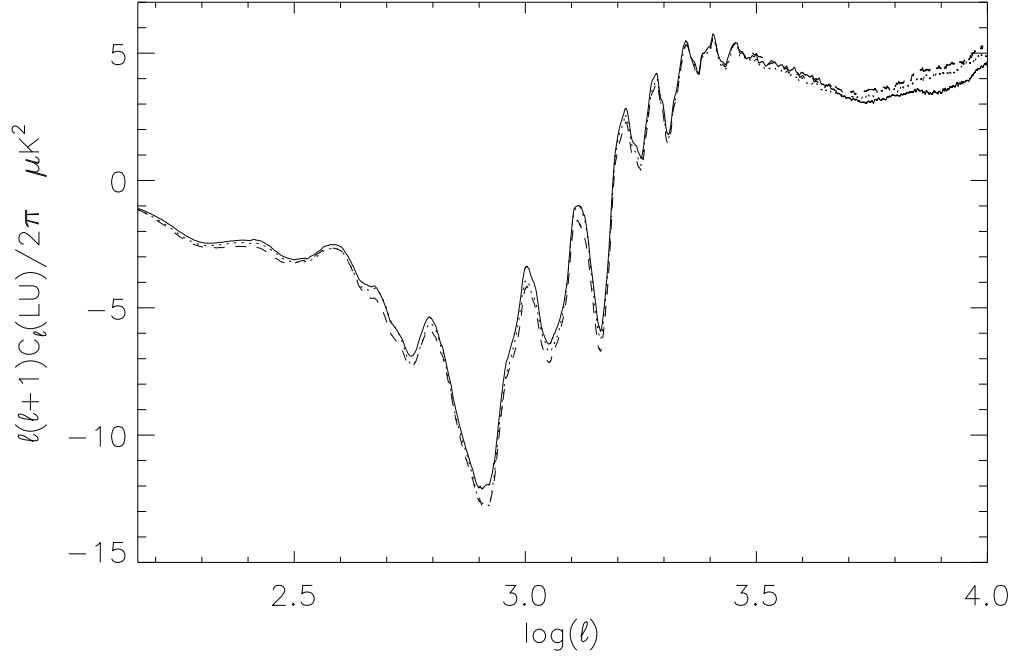


Fig. 8.— LU angular power spectra extracted for RLS_BA (solid line), and from other two LSs with the same parameters and initial conditions, but differing softenings and photon steps where, $\Delta_{ps} = 50h^{-1} \text{ kpc}$ and $S_p = 24h^{-1} \text{ kpc}$ (LS_ΔS1AA, dotted line), and $\Delta_{ps} = 75h^{-1} \text{ kpc}$ and $S_p = 36h^{-1} \text{ kpc}$ (LS_ΔS2AA, dashed line).

distinct sets of initial modes, giving rise to four LSs. The four spectra for each Δ_{ps} value were then averaged and the resulting spectra plotted in Fig. 9. Note, that since the error in the lensing deviation integrals is reduced with decreasing Δ_{ps} , we can reasonably argue that our best estimate of the lensing signal is given by the minimum Δ_{ps} . We see that in all three cases the $C_\ell(LU)$ quantities are in close agreement up to $\ell \sim 7000$. In the ℓ -interval [7,000–10,000], the separations between the three curves increase, with a systematic trend of a lower signal with decreasing photon-step. Since all these spectra have the same simulation softening it is reasonable to conclude that the trend we observed when comparing different S_p and Δ_{ps} may actually be a function of the change in Δ_{ps} . Given that the smallest Δ_{ps} exhibits the lowest signal, we thus conclude that our best estimate of the signal actually has the smallest correlations for $\ell > 7000$ values. Nonetheless, for $\ell < 7000$, the RLS closely follows our best estimate, hence for $\ell < 7000$ we are very confident that the RLS leads to a robust estimate of the lensing effect we are studying. Even if the $\Delta_{ps} = 12h^{-1} \text{ kpc}$ value leads to the most accurate spectrum (which is not certain), the computational cost of constructing these LSs is significantly greater than that of the RLSs, while only providing a mild improvement in accuracy for $\ell > 7000$.

We have also attempted to reproduce results similar to that found elsewhere using interpolation methods. We ran another simulation using RLS_AA parameters, except that this time the deflections were calculated using the 8 nearest neighbours. This keeps the mass resolution of the simulation fixed and does not alter the gravitational calculation, while at the same time lowering the effective resolution of the lensing methodology. The resulting power spectrum is shown in Fig. 10 and shows a decaying signal at high ℓ which is similar to that found in earlier work (*e.g.* Das & Bode (2008)). This shows that as we degrade the resolution of ray-tracing method we do indeed recover previous results.

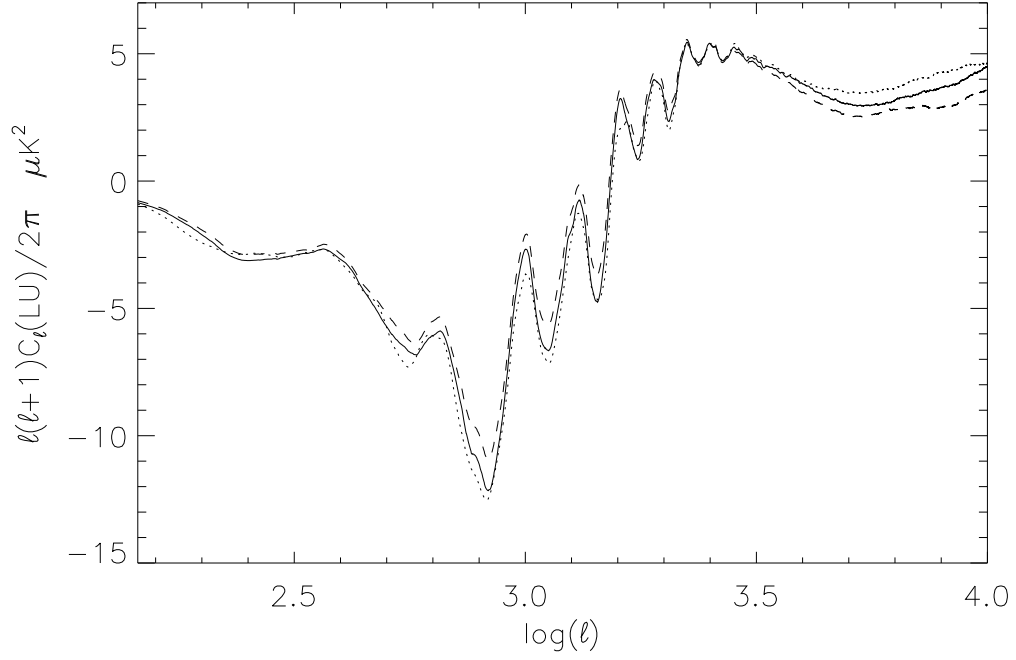


Fig. 9.— Average LU angular power spectra extracted from RLSs (solid line), and from other two LSs with the same parameters, excepting the photon step Δ_{ps} , whose values are $\Delta_{ps} = 40h^{-1} \text{ kpc}$ (dotted line) and $\Delta_{ps} = 12h^{-1} \text{ kpc}$ (dashed line). The dashed, solid, and dotted lines corresponds to the smallest, medium (RLS), and greatest Δ_{ps} values, respectively. Averages have been performed by using four appropriate simulations (see text).

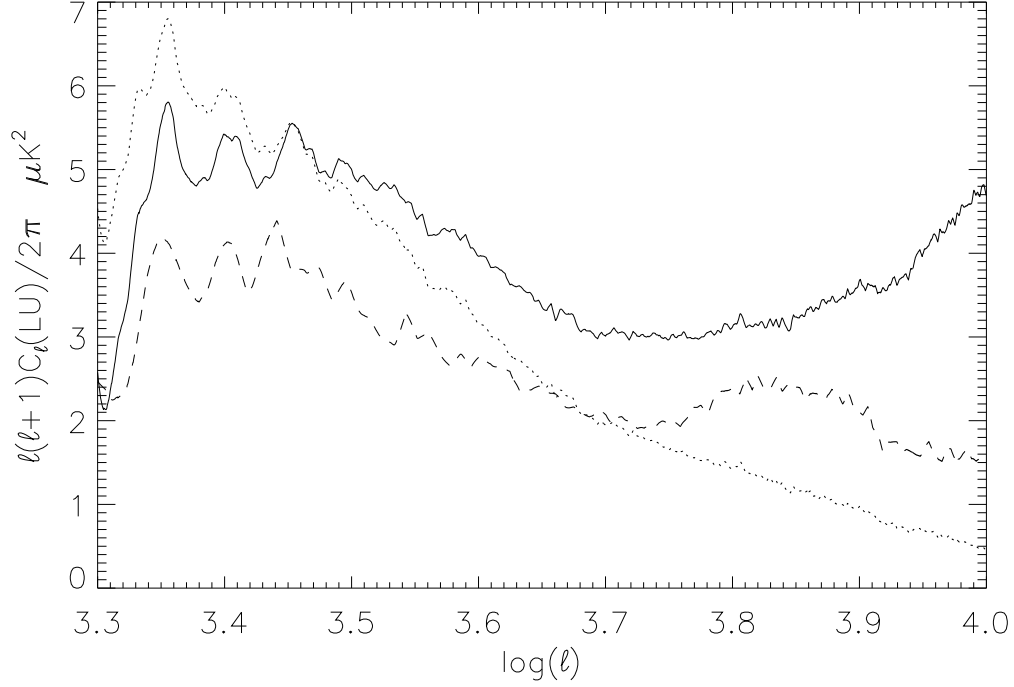


Fig. 10.— LU angular power spectra for the RLS_AA simulation (solid line) as compared to the same simulation but where deflections are calculated by including an average over the 8 nearest geodesics (dotted line). This reduces the resolution of geodesic method, but maintains the same resolution in the gravitational solver. Also shown (dashed line) is the highest resolution (but small volume) LS_HEA simulation. As shown in more detail in figure 11, higher resolution reduces the impact of discreteness effects, which in turn reduces the asymptotic high ℓ signal. However, sample variance issues in the LS_HEA simulation preclude us for drawing firm conclusions at present.

4.8. Impact of mass resolution on convergence

Since our ray-tracing method samples the local gravitational field on scales down to a few tens of kpc, it is important to investigate the role of mass resolution on our simulation. While we have investigated box size earlier, which at a fixed resolution leads to a change in mass resolution, in this section we focus on changing the mass resolution in a fixed volume, and also include one additional simulation in a smaller volume at our maximum mass resolution.

We ran additional simulations with 128^3 and 256^3 particles in the RLS box size, namely $512h^{-1}$ Mpc. These simulations are labeled LS_LHA and LS_MGA in Table 1. Notable other parameters were $S_p = 48h^{-1}(24h^{-1})$ kpc, $\Delta_{ps} = 120h^{-1}(60h^{-1})$ kpc and particle masses were $7.0 \times 10^{12} (8.8 \times 10^{11}) M_\odot$ respectively. In Fig. 11 we plot the power spectrum results for these simulations, along with an RLS, another 512^3 simulation with a shorter photon step (LS_1AB), and one final simulation labeled LS_HEA that uses a volume 1/8th the size of an RLS but with the same number of particles. The parameters of this LS were $L_{box} = 256h^{-1}$ Mpc, $S_p = 6h^{-1}$ kpc and $\Delta_{ps} = 15h^{-1}$ kpc. Note the two 512^3 simulations have the same mass resolution but they bracket a range of photon-step values, a full estimate of the uncertainty in the signal at this mass resolution is given in Figure 13, where the spectra of these two cases appear inside the band of uncertainty. Due to the different box size of the LS_HEA run we could not maintain the same modes across all runs, and hence we used different initial modes at different resolutions. Taken together, these simulations span a ratio in mass resolution of 512.

The plot shows that when PP corrections are included there is a resolution-dependent up-turn in the power spectrum for $\ell > 5000$. Improving the mass resolution reduces the impact of N-body discreteness on the lensing (*e.g.* Jain et al. 2000) to the point where the highest resolution simulation (LS_HEA) appears to be free of this contamination for

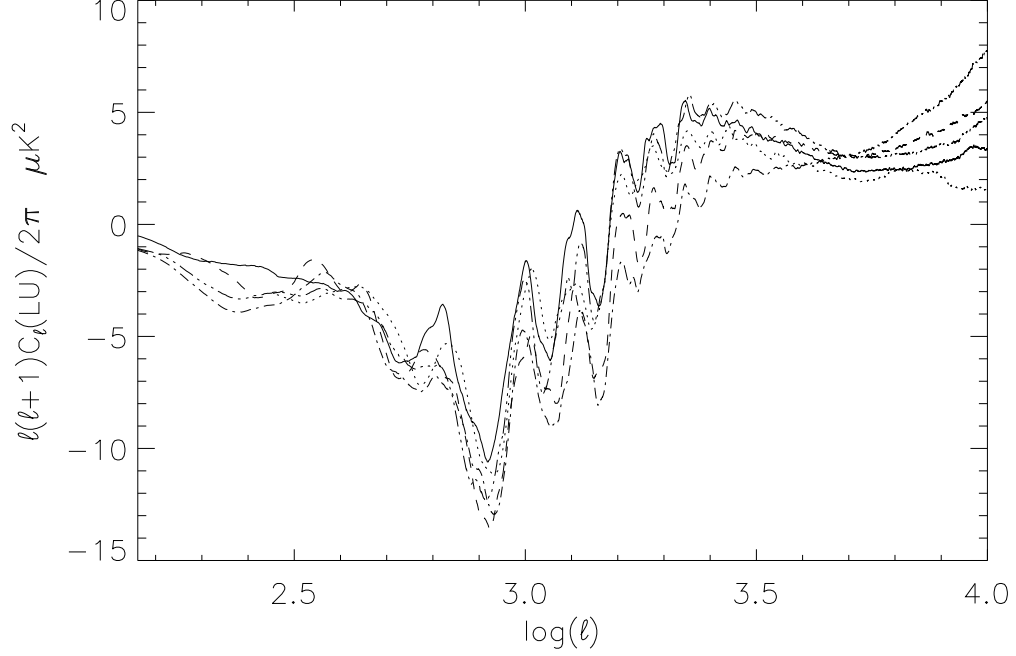


Fig. 11.— Comparison of convergence in the LU angular power spectra for different mass resolutions. The dot-dashed line corresponds to the 128^3 simulation LS_LHA, the dashed line to the 256^3 simulation LS_MGA, the triple-dot-dashed line to RLS_AA, the solid line to LS_Δ1AB, and the dotted line to LS_HEA. The simulation boxes are $512h^{-1}$ Mpc except for the LS_HEA simulation which uses 1/8th the volume. The two 512^3 simulations have the same mass resolution but they bracket a range of photon-step values (see Table 1 for simulation details), a full estimate of the uncertainty in the signal at this mass resolution is given in Figure 13.

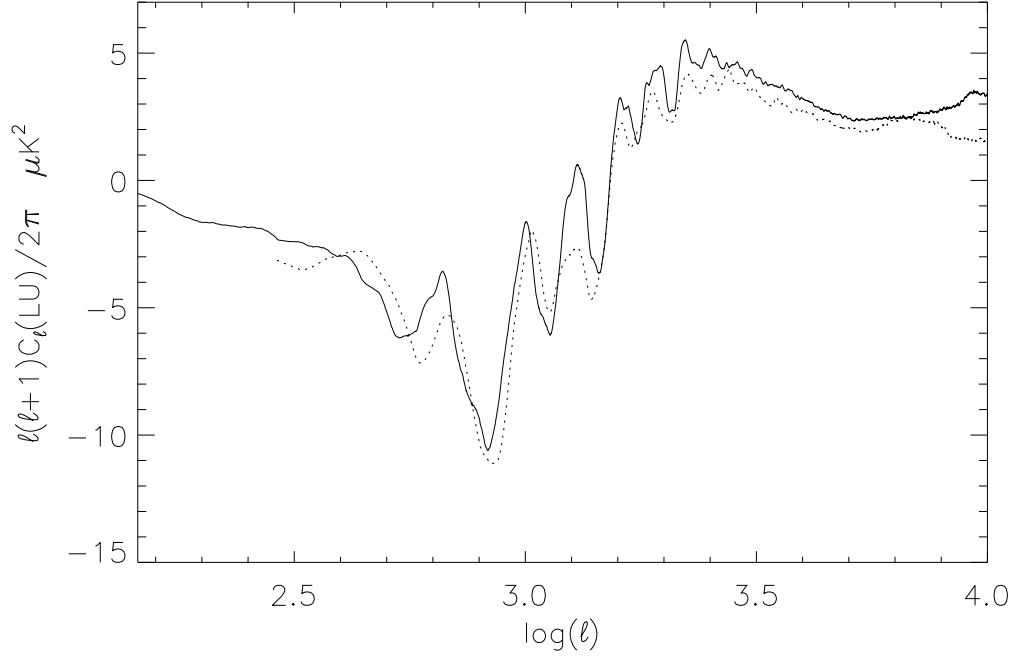


Fig. 12.— LU angular power spectra extracted from two LS obtained from fully independent initial conditions, but differing in short-scale resolution. The dotted line corresponds to LS_HEA with parameters $L_{box} = 256h^{-1} \text{ Mpc}$, $N_p = 512^3$, $N_c = 1024$, $N_{dir} = 512$, $S_p = 6 \times 10^{-3}h^{-1} \text{ Mpc}$, and $\Delta_{ps} = 15h^{-1} \text{ kpc}$. The solid line corresponds to LS_Δ1AB which has $\Delta_{ps} = 12 \text{ kpc}$ and the remaining parameters identical to those of the RLSs.

$\ell < 10^4$. Turning to lower ℓ values, the peak of the power spectrum around $\ell \sim 2000$ appears to be converged, modulo the variation due to the initial modes, for resolutions of 512^3 and greater. The results for $\ell < 1000$ also appear to show errors consistent with the variation in initial modes observed in Section 4.3, indicating results are converged in this range for all resolutions.

4.9. Is convergence at $\ell > 7000$ possible?

To address the question of the correct form of the spectrum at $\ell > 7000$ we utilize the RLSs and the LS_HEA simulation. The effective resolution $E_{res} \simeq 30h^{-1} \text{ kpc}$ of the LS_HEA simulation is half of that attained in the RLSs and thus small scales should be represented more accurately. As a result of the reduced box size, the angular size of the lensed maps is $\Phi_{map} = 2.48^\circ$ and the angular resolution limit $\Delta_{ang} = 0.29'$ ($\ell \sim 37000$) is half that of the RLSs (*i.e.* higher resolution).

The resulting spectrum is plotted in Fig. 12 as a dotted line, and compared to our previous best estimate for the signal at $\ell > 7000$, namely that from LS_Δ1AB that was constructed with $\Delta_{ps} = 12h^{-1} \text{ kpc}$ and the remaining parameters identical to those of the RLSs (the preferred direction is D512B). As expected, given that the new spectrum is obtained from smaller $2.48^\circ \times 2.48^\circ$ maps, some uncertainties in the $C_\ell(LU)$ quantities are observed for $\ell < 2000$. Note that for the $4.96^\circ \times 4.96^\circ$ maps used in the RLS we expect uncertainties for $\ell < 1000$. However, for $\ell > 2000$, the spectrum of the smaller box (dotted line) is expected to be more accurate than our previous LS. Although we again observe a systematic trend of better resolution producing a lower signal at high $\ell > 7000$, the results are nonetheless in good quantitative agreement for $2000 < \ell < 7000$. We can hence be confident that our RLSs give also a rough but useful estimate of the angular power spectrum for $2000 < \ell < 7000$ (supporting our assertion in the previous section). Finally,

for $7000 < \ell < 10,000$, the smaller box produces a decrease, whereas the previous LS increases slightly. This unfortunately suggests that the N-body simulations and the CMB lensed maps used to derive the RLSs are not good enough for $\ell > 7000$. We hence conclude that future simulations with higher resolutions are clearly necessary to go beyond $\ell = 7000$.

5. Discussion and observational implications

To bring together all that we have learned thus far, in Fig. 13 we plot all the LU angular power spectra from our simulations (excepting simulation LS_LHA with $N_p = 128^3$ particles) in the $\log(\ell)$ -interval (3.5, 4.0), which we reemphasize corresponds to the AWL effect described earlier (scales smaller than $42h^{-1} \text{ Mpc}$ at $z < 6$). The AWL and the complementary lensing effect BWL estimated with CMBFAST are also included in the same plot. Since we demonstrated the CWL component is negligible in the interval under consideration (see the bottom left panel of Fig 1), it is not represented. The lower solid line displays the same spectrum as the dotted line of Fig. 12, which corresponds to the LS_HEA LS, which has the smallest value of S_p and the highest mass resolution considered (eight times better than that of the RLSs). The upper solid line shows the same spectrum as the dashed line of Fig. 8, which corresponds to the LS_ΔS2AA LS, which has the same mass resolution as the RLSs but an S_p value 3 times larger (and 6 times larger than that used in the LS_HEA LS). Despite the large differences in the numerical parameters defining the N-body simulations, we see that from $\ell \simeq 3000$ to $\ell \simeq 7000$, all the spectra lie in a narrow band (bounded by the solid lines of Fig. 13), having a width close to half a micro-Kelvin. In addition to the simulation lines (solid and dotted) we have plotted estimates of the lensing signal based upon semi-analytical approaches implemented in the CMBFAST code (Lewis & Challinor 2006). By using the nonlinear version of this code with a minimum scale of $30h^{-1} \text{ kpc}$ (as in our LS, leading to the lower solid line of Fig. 13), we have estimated

the *AWL* (dash-dots line in Fig. 13 and top left panel of Fig. 1) and the *BWL* components (dashed line in Fig. 13 and top right panel of Fig. 1) of the weak lensing. Finally, the CMBFAST code has been also used to calculate the CMB angular spectrum, in the absence of lensing, for the model described in Section 2 (dash-three-dots line).

The complementary effect *BWL*, not calculated within the simulation, is due to scales greater than $L_{max} = 42h^{-1} \text{ Mpc}$. While the absence of this power has significant consequences for small ℓ values we will now show (with CMBFAST) that in the interval we are examining it is small. If the scale $L_{max} = 42h^{-1} \text{ Mpc}$ is placed on the last scattering surface at ($z \simeq 1100$), it subtends an angle of $14'.63$. However, in Fig. 13 we are plotting ℓ values corresponding to angles of $\sim 3'.4$ and $\sim 1'$, *i.e.* considerably smaller than the scale set by L_{max} on the last scattering surface. By this reason, the power of the dashed line, which is due to the linear scales greater than L_{max} , is expected to be small in the $\log(\ell)$ -interval of Fig. 13. CMBFAST estimates have confirmed this smallness (dashed line of Fig. 13). Nevertheless, the *BWL* effect is very important for much smaller ℓ values (see bottom right panel of Fig. 1).

The complementary *CWL* effect (see the bottom left panel of Fig. 1) is too small to be significant in the $\log(\ell)$ -interval (3.5, 4.0). The *AWL* effect obtained with CMBFAST (nonlinear version) is shown in the dot-dashed line of Fig. 13. This effect appears to be smaller than the *AWL* effect numerically estimated here (with AP3M simulations), whose power is found to be close to $2 \mu K$ for $3000 < \ell < 7000$. The total lensing would be obtained by adding this power and that of the dashed line (*BWL* component). We thus see that the total lensing effect has a power of a few μK .

To compare this result with other simulation work, we turn to the work by Das & Bode (2008). Since our map-making method does not allow us to plot the lensed and unlensed C_ℓ we have converted their results (specifically those in their Figure 4) to the

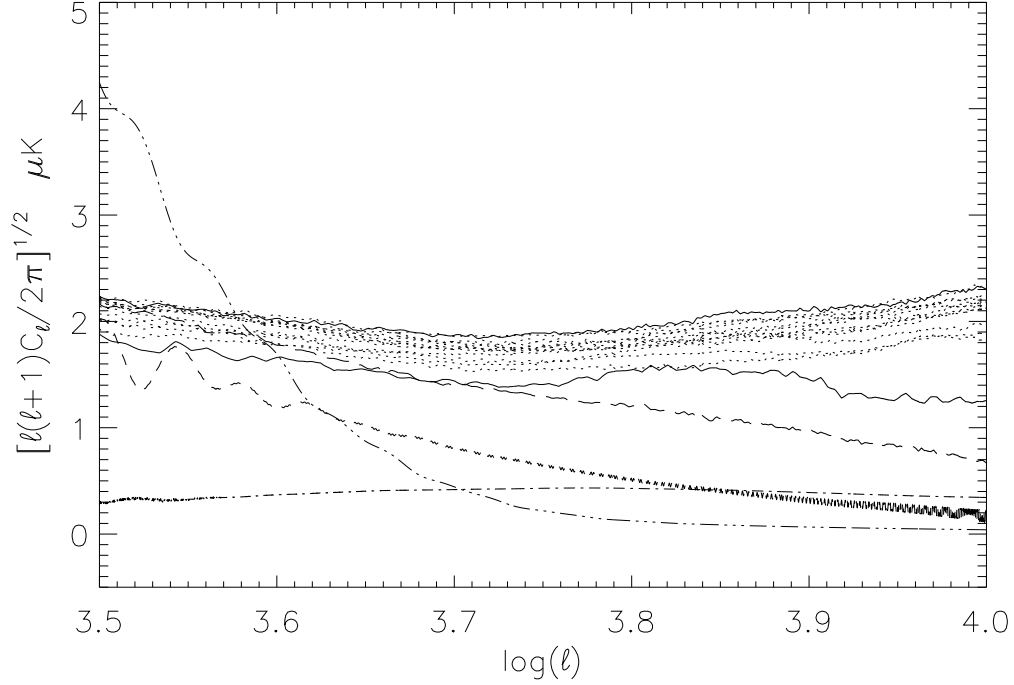


Fig. 13.— Angular power spectra, in μK , as functions of $\log(\ell)$. Solid and dotted lines represent all the spectra displayed in Figs. 4-12. The lower solid line displays the same spectrum as the dotted line of Fig. 12, which corresponds to the LS_HEA LS, which is the highest resolution simulation considered. The upper solid line shows the same spectrum as the dashed line of Fig. 8, which corresponds to the LS_ΔS2AA LS, which has the same mass resolution as the RLSs but an S_p value 3 times larger. The long dashed line corresponds to the geodesically averaged signal (mimicing reduced resolution), as shown in Figure 10. The dash-three-dot line is the CMB spectrum in the absence of lensing, and the dash-dot (dashes) line is the AWL (BWL) effect obtained with the CMBFAST code in the case of nonlinear lensing including structures with sizes $L > 30h^{-1} \text{ Kpc}$.

$[\ell(\ell+1)C_\ell(LU)/(2\pi)]^{1/2}$ values we use in our paper. In performing this conversion we have multiplied their power spectra by a factor of $2.90 \times 10^{13} \mu\text{K}^2$ which includes the effective fractional sky coverage, f_{sky}^{eff} . We hence find values of $1.1 \mu\text{K}$ at $\ell = 4000$, $0.7 \mu\text{K}$ at $\ell = 5000$, $0.6 \mu\text{K}$ at $\ell = 6000$ and $0.4 \mu\text{K}$ at $\ell = 7000$. This compares with our own signal of $2.0 \pm 0.4 \mu\text{K}$ across the entire range. However, we caution against over-interpreting this comparison. Our cosmology and assumptions about reionization and backgrounds are slightly different from those in Das & Bode (2008), however it is clear that we find a higher signal at $\ell > 1000$ when short range corrections are included.

As it is apparent from Fig. 13, the *AWL* effect clearly dominates the primary anisotropies for $\ell > 4200$ (*i.e.* the continuous and dotted lines are well above the dash-three-dots one). However, the Sunyaev-Zel’dovich (SZ) effect is also important at these scales, and foregrounds must be properly accounted for. The Berkeley-Illinois-Maryland Association (BIMA), has reported (Dawson *et al.* 2006) a temperature power $([\ell(\ell+1)C_\ell/2\pi]^{1/2})$ of $14.88_{-4.88}^{+4.09} \mu\text{K}$ at 68 % confidence, for $\ell = 5237$. In order to explain $14.88 \mu\text{K}$ as an SZ effect, one must have $\sigma_8 \simeq 1.03$ (Cooray 2002; Dawson *et al.* 2006), but this is in comparatively strong disagreement with data from WMAP (see Section 1) that lead to $\sigma_8 \simeq 0.82$. Hence, taking into account that the SZ temperature power scales as $\sigma_8^{3.5}$ (Komatsu & Seljak. 2002; Bond *et al.* 2005; Dawson *et al.* 2006; Sievers *et al.* 2009), the SZ effect could only explain around the 44.5 % of the most likely BIMA value ($14.88 \mu\text{K}$). The Cosmic Background Imager (CBI) observations, Bond *et al.* (2005), cover the multipole range $400 < \ell < 4000$ and, in a recent analysis (Sievers *et al.* 2009), it is argued that, if the CBI excess power observed at very small angular scales is explained as a SZ effect for a certain σ_8 value, then a power close to $10 \mu\text{K}$, marginally compatible with BIMA measurements at $\ell = 5237$, may be explained with the same value of σ_8 .

The level of power we predict for the weak lensing (*AWL* plus *BWL* components)

may thus be a missing link, simultaneously ensuring the compatibility of WMAP, CBI and BIMA observations. We have predicted a lensing effect of a few micro-Kelvin for these large angular scales, and hence a smaller SZ component (a smaller value of σ_8) could lead to simultaneous compatibility with WMAP, CBI, and BIMA observations. Aside from the large errors bars on the BIMA measurement, we are also cautious about making firm claims since lensing and SZ effects are essentially produced by the same structure distributions (galaxy clusters and sub-structures involving dark matter and baryons) and, consequently, these effects must be strongly correlated. This implies that the spectra of these two effects must be superposed in an unknown way (not merely added). In practice, this superposition might be analyzed in detail with ray-tracing through hydrodynamical simulations (including both baryons and dark matter). More work along these lines is clearly necessary.

6. Conclusions

Our first conclusion, in agreement with other work, is that PM simulations are inefficient for calculating CMB lensing due to strongly nonlinear structures (see Fig. 3 and comments in Section 4.2). While it is not impossible to simulate these effects with a PM code the required resolution is so large that the additional short-scale resolution provided by AP3M (or other high resolution N-body technique) is far more efficient at capturing the lensing effect. Hence our development of a combined parallel AP3M-ray-tracing code is a necessary step to estimate the lensing signal at high ℓ .

Only the *AWL* effect (see Section 3) produced by scales smaller than $42h^{-1} \text{ Mpc}$ between redshifts $z_{in} = 6$ and $z_{end} = 0$ has been estimated with AP3M simulations. This choice is appropriate for the following reasons: (1) all the strongly nonlinear scales are taken into account; (2) omitting scales greater than $42h^{-1} \text{ Mpc}$ makes our ray-tracing procedure efficient (see Section 3); (3) the effect produced by scales greater than $42h^{-1} \text{ Mpc}$ (*BWL* in

Section 3) can be studied by using the linear version of CMBFAST; and, (4) the lensing due to scales smaller than $42h^{-1} \text{ Mpc}$, at redshift $z > 6$ (*CWL* in Section 3), can be computed using standard semi-analytical methods implemented in CMBFAST.

Given that our study has strongly focused on the *AWL* signal, we exhaustively investigated the numerical issues involved when estimating this signal. Our main conclusions can be summarized as follows:

- the lensing contribution between $z = 0.2$ and $z = 0$ is negligible
- for each RLS, a few realizations suffice to get a good average $C_\ell(LU)$ spectrum and, moreover, each single simulation gives a very good spectrum rather similar to the average one
- RLSs, which are essentially identical except for the preferred directions, give similar spectra (the ray-tracing procedure has little variance)
- simulation boxes of $1024h^{-1} \text{ Mpc}$ are not fully necessary for $\ell > 1000$; however, for $\ell < 1000$, these large sizes lead to the most reliable spectra and, moreover, such sizes should lead to very good spectra in the ℓ -interval (1000–2000)
- simulations in boxes of $512h^{-1} \text{ Mpc}$ lead to good $C_\ell(LU)$ spectra for $1000 < \ell < 7000$
- for $2000 < \ell < 7000$, all the RLSs lie in a region of width $\sim 0.5 \text{ } \mu\text{K}$, indicating that the RLSs give consistent estimates of the signal in this range
- the signal in the range $4000 < \ell < 7000$ is $2.0 \pm 0.4 \text{ } \mu\text{K}$, which is $\sim 1.4 \text{ } \mu\text{K}$ higher than that found elsewhere (*e.g.* Das & Bode 2008)

Despite some simulation uncertainties, our code and technique have lead to a robust estimate of the lensing effect in the ℓ -interval (4200, 7000), where it clearly dominates

the primary anisotropy. Moreover, the estimated power is larger than that obtained with semi-analytical methods and the CMBFAST code. We thus suggest that the resulting value of a few micro-Kelvin may explain the excess power at high ℓ in the BIMA and CBI observations. This conclusion is supported by recent studies based on the Millennium simulation (Carbone *et al.* 2008), where the authors have reported a small contribution from nonlinearity at $\ell \simeq 4100$. However, the methods of Carbone *et al.* (2008) have been designed to build all-sky lensed maps, and do not have the resolution necessary to perform an accurate estimate of the weak lensing by strongly nonlinear structures in the ℓ -interval where we have found our main effect.

Our direct estimation of the potential gradients at photon positions using PP corrections from the local dark matter particles appears to be the main origin of the difference between our results and other research relying either on planes or grid interpolations. However, we emphasize that differences only occur at the large $\ell > 2000$ values we have been investigating. Our method employs extremely fine time resolution, namely that used by AP3M simulations and also a very good angular resolution (see above). Due to current limitations in our method it is not possible for us to determine the precise role of temporal resolution in an accurate lensing calculation.

It is well known that on small scales baryons do not follow the dark matter distribution. Thus, while we have attempted to be as accurate as possible in this dark matter simulation, we are now probing scales where contributions from baryons are beginning to become significant. An investigation of the impact of baryons by Jing *et al.* (2006) considered two types of simulations, the first with non-radiative baryons while the second included dissipation and star formation. They found that for $1000 < l < 10,000$ an effect of between 1% to 10% on the weak-lensing shear angular power spectrum, as calculated from dark matter alone, was possible. The largest difference was produced in the run with dissipation

and star formation, where a 10% increase in the (shear) C_ℓ s at $\ell = 10000$ was observed. Future work is definitely necessary to determine the impact of this physics on lensing statistics. We plan to conduct simulations with baryons and feedback processes both to identify its impact on the signal we find, and also to systematically evaluate the combined impact of the SZ effect and weak lensing.

For calculations that are accurate to high ℓ it seems to be necessary to move CMB photons through the simulation box while structures are evolving, which ensures the spatial gradients are accurately calculated on the photon positions (test particles). Once the N-body code has been modified to compute spatial gradients at particle test positions, there are no theoretical or technical reasons to take a temporal resolution different from that defined by the simulation time step. From the theoretical point of view, the time step resolution is obviously most compatible with the N-body technique (and thus takes into account the entire evolution of the simulation). From the technical point of view, the use of the time step resolution requires the minimum memory cost as the number of test particles between two successive times, although large, is minimized. Because of these considerations, temporal resolution is not a parameter to be varied in our calculations.

Our AP3M code adapted to CMB lensing calculations can be run for different values of the parameters defining the LSs; hence, this code allows us to see how the resulting angular power spectra depend on the parameters defining both the N-body simulation and the ray-tracing procedure.

We thank the anonymous referee for suggestions that improved the clarity and content of the paper. M.J. Fullana, J.V. Arnau and D. Sáez acknowledge the financial support of the Spanish Ministerio de Educación y Ciencia, MEC-FEDER project FIS2006-06062. RJT and HMPC acknowledge funding by individual Discovery Grants from NSERC. RJT is also supported by grants from the Canada Foundation for Innovation and the Canada Research

Chairs Program. HMPC acknowledges the support of the Canadian Institute for Advanced Research. Simulations were performed at the *Computational Astrophysics Laboratory* at Saint Mary’s University.

REFERENCES

- Antón L., Cerdá-Durán, P., Quilis, V., and Sáez, D. 2005, ApJ, 628, 1
- Arnau J.V., Aliaga, A., and Sáez, D. 2002, A&A, 382, 1138
- Bond, J.R. *et al.*, 2005, ApJ, 626, 12
- Burigana, C., and Sáez, D. 2003, A&A, 409, 423
- Carbone, C., Springel, V., Baccigalupi, C., Bartelmann, M., & Matarrese, S., 2008, MNRAS, 388, 1618
- Carbone, C., Baccigalupi, C., Bartelmann, M., Matarrese, S., and Springel, V., 2009, MNRAS, 396, 668
- Cerdá-Durán, P., Quilis, V., and Sáez, D. 2004, Phys. Rev. D, 69, 043002
- Cooray, A., and Melchiorri, A. 2002, Phys. Rev. D, 66, 083001
- Couchman, H. M. P., 1991, ApJ, 368, 23
- Das, S., & Bode, P., 2008, ApJ, 682, 1
- Dawson, K.S., Holzapfel, W.L., Carlstrom, J.E., Joy, M., and LaRoque, S.J., 2006, ApJ, 647, 13
- Efstathiou, G., Davis, M., White, S. D. M. & Frenk, C., 1985, ApJS, 57, 241
- Fosalba, P., *et al.*, 2008, MNRAS, 391, 435
- Górski, K.M., Hivon, E., and Wandelt, B.D. 1999, in Proc. MPA/ESO Cosmology Conf., ed. A.J. Banday, R.K. Sheth and L. N. da Costa (Garching: European Southern Observatory) (astro-ph/9812350)

- Hamana, T., *et al.*, 2001, A&A, 367, 18
- Harrison, E. R., 1970, Phys. Rev. D., 1, 2726
- Hernquist, L. & Katz, N., 1989, ApJS, 70, 419
- Hilbert, S., *et al.*, 2009, A&A, 499, 31
- Hinshaw, G., et al., arXiv:0803.0732
- Hockney R.W., and Eastwood J.W. 1988, Computer Simulations Using Particles (Bristol: IOP)
- Jain, B., Seljak, U., and White, S. 2000, ApJ, 530, 547
- Jing, Y. P., Zhang, P., Lin, W. P., Gao, L., and Springel, V., 2006, ApJ, 640, L119
- Knox, L. 1995, Phys. Rev. D, 52, 4307
- Kim, J., *et al.*, 2008, arXiv:0812.1392
- Komatsu, E., & Seljak, U. MNRAS, 336, 1256
- Komatsu, E., et al., arXiv:0803.0547
- Lewis, A., and Challinor, A. 2006, Phys. Rep., 429, 1
- Moore, B., Governato, F., Quinn, T., Stadel, J., & Lake, G., 1998, ApJ, 499, L5
- Moutarde, F., Alimi, J.-M., Bouchet, F.R., Pellat, R., and Ramani, A. 1991, ApJ, 382, 377
- Perlmutter, S., *et al.* 1999, ApJ, 517, 565
- Puchades, N., Fullana, M.J. Arnau, J.V. and Sáez, D. 2006, MNRAS, 370, 1849
- Quilis, V., Ibáñez, J.M., and Sáez, D. 1998, ApJ, 502, 518

- Riess *et al.* 1998, AJ, 116, 1009
- Sáez, D., Holtmann, E., and Smoot, G.F. 1996, ApJ, 473, 1
- Sáez, D., Puchades, N., Arnau, J.V. and Fullana, M.J. 2006, Proceedings of Science, 058
- Sandarin, S.F., and Zel’dovich, Ya. B. 1989, Rev. Mod. Phys., 61,185
- Sato, M., *et al.* , 2009, arXiv:0906.2237
- Scott, D., Srednicki, M. and White, M. 1994, ApJ, 421, L5
- Seljak, U., and Zaldarriaga, M. 1996, ApJ, 469, 437
- Seljak, U. 1996, ApJ, 463, 1
- Shapiro, C., & Cooray, A., 2006, JCAP, 603, 7
- Sievers, J.L., *et al.* , 2009, arXiv:0901.4540
- Smith, R.E, *et al.* 2003, MNRAS, 341, 1311
- Spergel, D. *et al.* 2007, ApJS, 170, 377
- Springel, V., *et al.* , 2005, Nature, 435, 629
- Teyssier, R., *et al.* , 2009, A&A, 497, 335
- Thacker, R. J., & Couchman, H. M. P., 2006, Comp. Phys. Comm., 174, 540
- Van Waerbeke, L., *et al.* , 2001, MNRAS, 322, 918
- Vianna, P. T. P. & Liddle, A. 1996, MNRAS, 281, 323
- White, M., and Hu, W. 2000, ApJ, 537, 1
- Zel’dovich, Ya. B. 1970, A&A, 5, 84

